

MagSAF: software for simulating and fitting magnetic hysteresis loops of synthetic antiferromagnets

Stephan Glamsch, Matthias Küß, Afan Terko, Andreas Hörner, Erol Girt, Manfred Albrecht

Angaben zur Veröffentlichung / Publication details:

Glamsch, Stephan, Matthias Küß, Afan Terko, Andreas Hörner, Erol Girt, and Manfred Albrecht. 2025. "MagSAF: software for simulating and fitting magnetic hysteresis loops of synthetic antiferromagnets." *Journal of Applied Physics* 138 (20): 203901. <https://doi.org/10.1063/5.0288886>.

Nutzungsbedingungen / Terms of use:

CC BY 4.0

Dieses Dokument wird unter folgenden Bedingungen zur Verfügung gestellt: / This document is made available under these conditions:

CC-BY 4.0: Creative Commons: Namensnennung

Weitere Informationen finden Sie unter: / For more information see:

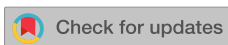
<https://creativecommons.org/licenses/by/4.0/deed.de>



RESEARCH ARTICLE | NOVEMBER 24 2025

MagSAF: Software for simulating and fitting magnetic hysteresis loops of synthetic antiferromagnets

Stephan Glamsch ; Matthias K    ; Afan Terko; Andreas H  rner; Erol Girt; Manfred Albrecht 



J. Appl. Phys. 138, 203901 (2025)

<https://doi.org/10.1063/5.0288886>



Articles You May Be Interested In

Magnetic field induced spin wave reflection by a domain wall in synthetic antiferromagnets

J. Appl. Phys. (August 2024)

Implementation of a full Wheatstone-bridge GMR sensor by utilizing spin-orbit torque induced magnetization switching in synthetic antiferromagnetic layer

J. Appl. Phys. (April 2023)

XPS depth profiling of an ultrathin bioorganic film with an argon gas cluster ion beam

Biointerphases (May 2016)

10 December 2025 12:45:04

Nanotechnology & Materials Science

Optics & Photonics

Impedance Analysis


Scanning Probe Microscopy

Sensors


Failure Analysis & Semiconductors

Unlock the Full Spectrum.
From DC to 8.5 GHz.

Your Application. Measured.



[Find out more](#)



MagSAF: Software for simulating and fitting magnetic hysteresis loops of synthetic antiferromagnets

Cite as: J. Appl. Phys. **138**, 203901 (2025); doi: [10.1063/5.0288886](https://doi.org/10.1063/5.0288886)

Submitted: 3 July 2025 · Accepted: 3 November 2025 ·

Published Online: 24 November 2025



Stephan Glamsch,^{1,a)} Matthias Küß,¹ Afan Terko,² Andreas Hörner,¹ Erol Girt,² and Manfred Albrecht¹

AFFILIATIONS

¹Institute of Physics, University of Augsburg, 86159 Augsburg, Germany

²Department of Physics, Simon Fraser University, Burnaby, British Columbia V5A 1S6, Canada

^{a)}Author to whom correspondence should be addressed: stephan.glamsch@uni-a.de

ABSTRACT

We have developed the macrospin-based software MagSAF that allows for fast and easy simulations of magnetic hysteresis loops of synthetic antiferromagnets with in-plane magnetization and in-plane uniaxial magnetic anisotropies. Additionally, the bilinear and biquadratic interlayer exchange coupling strengths can be extracted from experimental data via curve fitting. It also nurtures understanding the physics behind the magnetic hysteresis loops by allowing the user to examine the macrospin angle rotation and the energy landscape during the magnetic field sweep. We prepared CoFeB(5 nm)/Ru(d_{Ru})/CoFeB(5 nm) synthetic antiferromagnets with $0.4 \text{ nm} \leq d_{\text{Ru}} \leq 0.85 \text{ nm}$ to test our software. We find great agreement between our extracted bilinear and biquadratic coupling strengths and those that were obtained with a more advanced discrete energy model that takes the twisting of spins over the ferromagnetic layer thickness into account. For a thicker synthetic antiferromagnet CoFeB(18.0 nm)/Ru(0.55 nm)/CoFeB(5.75 nm), the differences between the macrospin and discrete energy model become more apparent.

© 2025 Author(s). All article content, except where otherwise noted, is licensed under a Creative Commons Attribution (CC BY) license (<https://creativecommons.org/licenses/by/4.0/>). <https://doi.org/10.1063/5.0288886>

I. INTRODUCTION

Synthetic antiferromagnets (SAFs) consist of two ferromagnetic (FM) layers, which are separated by a very thin non-magnetic (NM) spacer layer and couple antiferromagnetically. The spacer layer introduces an indirect interlayer exchange coupling (IEC) with two coupling terms: the bilinear J_{bl} and biquadratic J_{bq} coupling. For both coupling terms, there are a few theoretical models that attempt to explain their physical origin. The quantum interference model seems to be the best physical description of the bilinear IEC phenomenon.^{1,2} In this model, the interlayer exchange coupling arises from quantum interferences due to spin-dependent reflections of Bloch waves at the NM/FM interface. Historically, however, the bilinear coupling is often attributed to the Ruderman–Kittel–Kasuya–Yosida model^{3–5} because it was the first to accurately describe the oscillatory coupling behavior. The phenomenological biquadratic term was first introduced by Rührig *et al.*⁶ Until now, many different physical origins and possibilities

to actively influence it have been proposed, e.g., by thickness inhomogeneities of the NM layer,⁷ FM additions in the NM layer,^{8–10} dipolar fields due to a rough FM/NM interface,¹¹ and pinholes in the NM layer.¹² Some of these models are also summarized in Refs. 13 and 14. Finally, another roughness-induced coupling effect, Néel “orange-peel” coupling, can be present, which typically favors parallel alignment for in-plane (ip) magnetized FM layers.^{15–17}

The IEC influences both the static and dynamic magnetic properties of SAFs. Most commonly, the static behavior in the form of a magnetic hysteresis loop is used to extract the coupling strength of SAFs. However, the exact approach differs from publication to publication. Sometimes, only saturation or exchange fields are used to compare coupling strengths.^{18–23} Others fit their experimental hysteresis loops with a macrospin model to obtain an effective coupling strength J_{ex} ,^{24,25} while others fit the individual bilinear J_{bl} and biquadratic J_{bq} terms.^{26–34} Even though the macrospin model has several advantages compared to more complex

10 December 2025 12:45:04

models, such as its low computational cost and ease of understanding, one large limitation is its neglect of spin twisting over the FM film thickness. Since IEC is an interface effect, only the ferromagnetic spins at the FM/NM interface experience its coupling directly. It then depends on all energy contributions, i.e., Zeeman energy, anisotropies, and indirect and direct exchange interaction, whether the IEC favored alignment is continued through the FM film thickness or whether the spins start to twist away toward an energetically more favorable position. This spatial difference in spin orientation can be taken into account by dividing each FM layer into sublayers, which are coupled via direct exchange interaction.^{35–41}

Despite the relevance and many applications of SAFs,^{32,42–45} there is no easy-to-use open-source software available to simulate and fit magnetic hysteresis loops of SAFs. Only last year, Wadge *et al.*⁴⁰ released their discrete energy model, where each FM layer is divided into sublayers, together with a website for users to fit their data. However, this has some limitations, e.g., the user interface on their website can only be used for fits and not for individual simulations, and anisotropies are currently not implemented. We developed the macrospin-based open-source software MagSAF,⁴⁶ which has a simple user interface with the goal to act as a stepping stone for researchers who want to get into the field of SAFs. It enables researchers to simulate and fit magnetic hysteresis loops of SAFs with uniaxial magnetic anisotropies. Besides that, one can look at the macrospin rotation and energy landscape during the magnetic field sweep to better understand what is behind the magnetic hysteresis loop. By fitting experimental data, the bilinear and biquadratic IEC strengths can be obtained. We showcase this with a CoFeB(5)/Ru(d_{Ru})/CoFeB(5) (all thicknesses in nm) SAF thickness series and compare our extracted bilinear and biquadratic coupling strengths with those obtained with the discrete energy model. Finally, we stress test our macrospin model using a rather thick CoFeB(18.0 nm)/Ru(0.55 nm)/CoFeB(5.75 nm) SAF sample and compare our results again with the discrete energy model.

II. THEORY AND IMPLEMENTATION

In this work, we investigate thin film SAFs with magnetizations aligned in the plane of the SAF. This holds true for the often considered case of a prevailing thin film shape anisotropy and the external magnetic field being aligned in-plane (see Fig. 1). In the

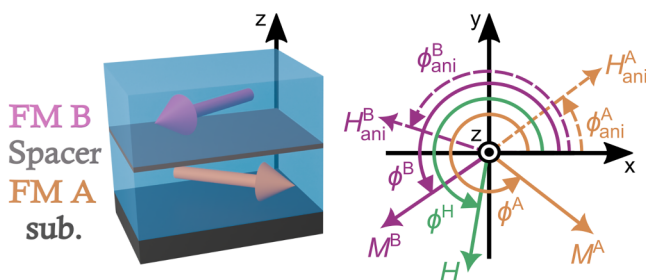


FIG. 1. Illustration of the layer structure of a synthetic antiferromagnet with arbitrary in-plane macrospin orientations and angle definitions.

macrospin model, all magnetic moments of one ferromagnetic layer are summed up to one “macro” spin M_s^i , i.e., the exchange stiffness is $A_{ex} = +\infty$. In our macrospin model, the total magnetic energy per unit area G of the SAF comprises the Zeeman energy, any in-plane uniaxial magnetic anisotropy of each ferromagnetic layer, and the bilinear and biquadratic energies arising from coupling between the layers. Thus, it can be formulated as

$$G = -d^A M_s^A \mu_0 [H \cos(\phi^A - \phi^H) + 0.5 H_{ani}^A \cos^2(\phi^A - \phi_{ani}^A)] - d^B M_s^B \mu_0 [H \cos(\phi^B - \phi^H) + 0.5 H_{ani}^B \cos^2(\phi^B - \phi_{ani}^B)] - J_{bl} \cos(\phi^A - \phi^B) - J_{bq} \cos^2(\phi^A - \phi^B), \quad (1)$$

where ϕ^i , d^i , M_s^i , H_{ani}^i , and ϕ_{ani}^i are the macrospin angle, thickness, saturation magnetization, uniaxial magnetic anisotropy field, and easy axis direction of the ferromagnetic layer $i = A, B$. μ_0 is the vacuum permeability, ϕ^H and H are the external field angle and magnitude, and J_{bl} and J_{bq} are the bilinear and biquadratic coupling strengths, respectively. In our definition, a negative J_{bl} value leads to antiferromagnetic coupling. Note that we neglect the demagnetization energy. Further, MagSAF does not currently offer the capability to simulate out-of-plane fields. Consequently, it is not able to simulate or fit out-of-plane easy-axis SAFs in its present form.

Figure 1 illustrates an arbitrary orientation of the macrospins of a SAF. For the simulation of the magnetic hysteresis loops, the equilibrium positions $\phi^{A,B}$ of the macrospins must be known. They are found at the local minima in the energy landscape $G(\phi^A, \phi^B)$. When the magnetic moments are saturated, we can assume that the equilibrium positions of the macrospins are along the external field $\phi^{A,B} = \phi^H$. For the simulation of a full magnetic hysteresis loop, the equilibrium positions of the previous field step H_{j-1} is used as a starting guess in the search for the new local minimum in the energy landscape $G(\phi^A, \phi^B)$ for the new field value H_j .

For the local minimizer, we use the open-source python package SciPy⁴⁷ and specifically its `scipy.optimize.minimize` function. Within this function, we use the built-in Newton-CG method, which is a line searching conjugate gradient method.⁴⁸ Even though this method takes both the Jacobian and Hessian matrix as input, which we can derive analytically, the minimizer gets stuck if the starting parameters for ϕ^A and ϕ^B lie on a saddle point or maximum in the current version of SciPy v1.15.2. This can become an issue, e.g., when coming from saturation, because it is possible that the equilibrium positions for ϕ^A and ϕ^B of the previous field step H_{j-1} are then lying on top of a saddle point for H_j and the local minimizer gets stuck. To circumvent this issue, we use the second partial derivative test. For that, instead of requiring G_{ϕ^A} (first derivative of G with respect to ϕ^A) and G_{ϕ^B} to be exactly 0, we allow for a small computational error by setting $|G_{\phi^A}| < 10^{-5}$ and $|G_{\phi^B}| < 10^{-5}$ as the first requirement because the local minimizer gets stuck or no longer minimizes even for very small non-zero gradients. Then, we check whether the determinant of the Hessian matrix is negative (saddle point) or whether the determinant of the Hessian matrix is positive and $G_{\phi^A \phi^A} < 0$ (second derivative of G with respect to ϕ^A) (maximum). If one of these is true, the algorithm searches through positions surrounding the previous equilibrium position for ϕ^A and ϕ^B in a spiral-like pattern, which is illustrated in Fig. 2.

10 December 2025 12:45:04

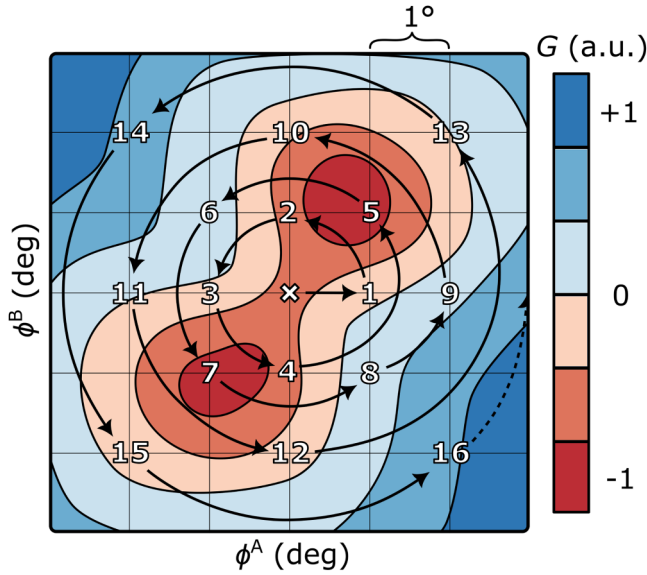


FIG. 2. Illustration of an energy landscape $G(\phi^A, \phi^B)$ zoomed in around a schematic saddle point. In this scenario, the starting guesses of the macrospin angles (cross) for the local minimizer lie on top of a saddle point. The `scipy.optimize.minimize` function would get stuck here. As a work-around, MagSAF checks surrounding positions (displayed here with numbers in ascending order) until the local minimizer is able to get off the saddle point (or maximum).

At every position (marked by numbers in Fig. 2), the Jacobian and Hessian matrix is calculated and the second partial derivative test is checked again. The first position where the test fails, i.e., where we are off the saddle point or maximum, is chosen as a new starting position for the local minimizer for the new field step H_j .

Once all equilibrium positions of the macrospin angles are known, the magnetic hysteresis is calculated using

$$M(H) = [d^A M_s^A \cos(\phi^A(H) - \phi^H) + d^B M_s^B \cos(\phi^B(H) - \phi^H)] / (d^A + d^B). \quad (2)$$

For fitting experimental hysteresis loops, MagSAF allows importing $M(H)$ data that has already been corrected for dia- or paramagnetic background signals and normalized to the magnetic volume. Refer to our GitHub documentation for more details.⁴⁶ After loading experimental hysteresis loops into MagSAF, they can be fitted by minimizing the figure of merit (FOM), which is defined as

$$\text{FOM} = \frac{1}{N} \sum_j \frac{\Delta H_j}{\Delta H_{\max}} \left| 1 - \frac{M_j^{\text{sim}}}{M_j^{\text{exp}}} \right|, \quad (3)$$

where \sum_j sums over all data points, N is the total number of data points, ΔH_j is equal to $|H_{j-1} - H_j| + |H_j - H_{j+1}|$, and ΔH_{\max} is the largest ΔH_j of the whole hysteresis loop. This first part eliminates over-weighting of specific field ranges where the field step size might be smaller (e.g., around zero field).

TABLE I. Sample name definitions with nominal thicknesses in nanometers. As substrate (sub) Y-cut LiNbO_3 was used. See Table S1 in the [supplementary material](#) for the table of the full series.

Sample	Layer stack
SYM2	sub/CoFeB(5)/Ru(0.5)/CoFeB(5)/ Si_3N_4 (3)
ASYM	sub/Ta(2)/Ru(2)/CoFeB(19)/Ru(0.55)/CoFeB(6)/ Si_3N_4 (3)

For the magnetic hysteresis fitting procedure, starting guesses and fit boundaries are used for the fit parameters. Because of this, if the starting guesses are completely off, it is possible that the fitting procedure will fail to produce a good result. In other words, if you imagine the multidimensional landscape of starting guesses vs the FOM of the result of the fitting procedure, it is possible that the starting guesses given by the user lie within a local minimum rather than a global one. Therefore, to ensure that the starting guesses lead to the best possible fit result (i.e., the smallest FOM), MagSAF first uses the global minimizer function `scipy.optimize.differential_evolution` to check that the starting guesses are close to the global minimum. Although it might seem counterintuitive, the starting guesses are not arbitrary because of this, but they influence the search region of the global minimizer. Hence, they should still be approximated as good as possible (e.g., by manually changing the parameters iteratively and simulating the hysteresis loop) before starting the fitting procedure. Finally, the best result of the global minimizer is then used as a new starting guess for a subsequent local minimizer `scipy.optimize.minimize(method=L-BFGS-B)`, which is constrained by the user-defined parameter boundaries. This is essentially the same as the `scipy.optimize.differential_evolution(polish=True)` option but instead we decided to run the `scipy.optimize.minimize(method=L-BFGS-B)` function separately to have more flexibility regarding its options. Note that we use the Newton-CG method, and not the L-BFGS-B method, to find the local minimum in the energy landscape $G(\phi^A, \phi^B)$ only because we found it to deliver better results for that particular problem via trial and error. Determining which optimizer is better suited for which problem is a research field in itself,⁴⁹ which is beyond the scope of this work.

III. EXPERIMENTAL METHODS

Two SAF systems were fabricated by sputter deposition using the Bestec P450 system: Symmetric sub/CoFeB(5)/Ru(d_{Ru})/CoFeB(5)/ Si_3N_4 (3) (SYM1-7) and asymmetric sub/Ta(2)/Ru(2)/CoFeB(19)/Ru(0.55)/CoFeB(6)/ Si_3N_4 (3) (ASYM) SAFs (with $\text{CoFeB} = \text{Co}_{40}\text{Fe}_{40}\text{B}_{20}$) (Table I). All samples were deposited on single-crystalline Y-cut LiNbO_3 substrates. For the symmetric SAF series SYM1-7, the Ru thickness was varied between 0.40 and 0.85 nm. The Si_3N_4 (3) capping layer protects the SAFs from oxidation. All metal layers were sputter-deposited at room temperature with a DC power supply at an Ar sputter pressure of 3.5 μbar and the Si_3N_4 layer with an RF power supply at 1.5 μbar with deposition rates of Ta 0.33 $\text{\AA}/\text{s}$, CoFeB 0.2 $\text{\AA}/\text{s}$, Ru 0.1 $\text{\AA}/\text{s}$, and Si_3N_4 0.08 $\text{\AA}/\text{s}$. The deposition rates were determined by a calibrated quartz oscillator

before deposition. The deposition was carried out at an oblique angle of approximately 20° toward the substrate surface normal, and the target–substrate distance was approximately 20 cm. For film thickness homogeneity, the substrate holder was rotated at 30 rounds per minute during deposition.

As expected, x-ray diffraction $2\theta/\omega$ scans confirmed that the CoFeB layers are amorphous (see the [supplementary material](#)). The ASYM sample was deposited one year prior to sample series SYM1-7, and the sputter targets were changed in the meantime. For ASYM, the CoFeB target was purchased from HMW Hauner with a purity of Fe 99.995%, Co 99.99%, and B 99.4%, and the Ru target was purchased from g-materials with a purity of 99.98%. For SYM1-7, the CoFeB target was also purchased from HMW Hauner with a purity of Fe 99.99%, Co 99.99%, and B 99.5% and the Ru target was purchased from Evochem Advanced Materials with a purity of 99.90%.

The magnetic hysteresis loops were measured using a superconducting quantum interference device–vibrating sample magnetometer (SQUID-VSM). Before measuring the samples, a $3 \times 4 \text{ mm}^2$ center piece of the original $4 \times 5 \text{ mm}^2$ samples was cut out with a wafer dicing saw to remove any magnetic material that was deposited on the substrate's sides during deposition. This was necessary specifically for the correct extraction of the saturation magnetization and in-plane uniaxial magnetic anisotropy.⁵⁰ Every sample was measured along two in-plane directions: the ip 0° direction is the crystallographic Z ([001] or [0001]) direction, and the ip 90° direction is the crystallographic X ([110] or [1120]) direction of the Y-cut LiNbO₃ substrate.⁵¹

IV. RESULTS AND DISCUSSION

A. Thin symmetric SAFs

First, the samples of the symmetric SAF thickness series are used to test our macrospin-based magnetic hysteresis fit software MagSAF. Additionally, the discrete energy model is utilized to

compare our fitting results with its more advanced sublayer approach that takes spin twisting over the FM thickness into account. Note that the symmetric SAF samples should only differ in their bilinear and biquadratic IEC strength. The fitting procedure for both models is explained in more detail in the [supplementary material](#).

In [Fig. 3\(a\)](#), the normalized experimental magnetic hysteresis loops of the SYM sample series are shown. Here, the change in saturation field H_s , which is directly proportional to the IEC strengths via

$$\mu_0 H_s = \underbrace{(J_{bl} + 2J_{bq})}_{J_{eff}} \left(\frac{1}{d^A M_s^A} + \frac{1}{d^B M_s^B} \right) \quad (4)$$

within the macrospin model,^{19,20,54} with the spacer layer thickness is already clearly visible. Note that [Eq. \(4\)](#) assumes that the in-plane anisotropy is zero. In [Figs. 3\(b\)](#) and [3\(c\)](#), experimental magnetic hysteresis loops and their fits are shown for $d_{Ru} = 0.50 \text{ nm}$ along the two in-plane directions ip 0° and ip 90° . The insets around zero field in [Figs. 3\(b\)](#) and [3\(c\)](#) show that the SAF possesses an in-plane uniaxial magnetic anisotropy with an easy axis (EA) along the ip 90° direction and that the SAF is slightly asymmetric. This has been found to be the case for all fabricated SAFs. The uniaxial magnetic anisotropy field strength is in the range of 1.10–3.29 mT and the $(d^A M_s^A - d^B M_s^B)/(d^A M_s^A + d^B M_s^B)$ asymmetry is in the range of 5.0%–7.4% for all symmetric SAF samples.

Let us first look into these two observations before we discuss the bilinear and biquadratic IEC strengths. The unexpected uniaxial magnetic anisotropy is often reported for sputter-deposited FM materials; however, its origin remains unclear. It is reported that stray fields from the magnetrons inside the sputter chamber could be the source,^{55–57} which seems unlikely in our case as the sample holder was rotating during deposition and the target–substrate

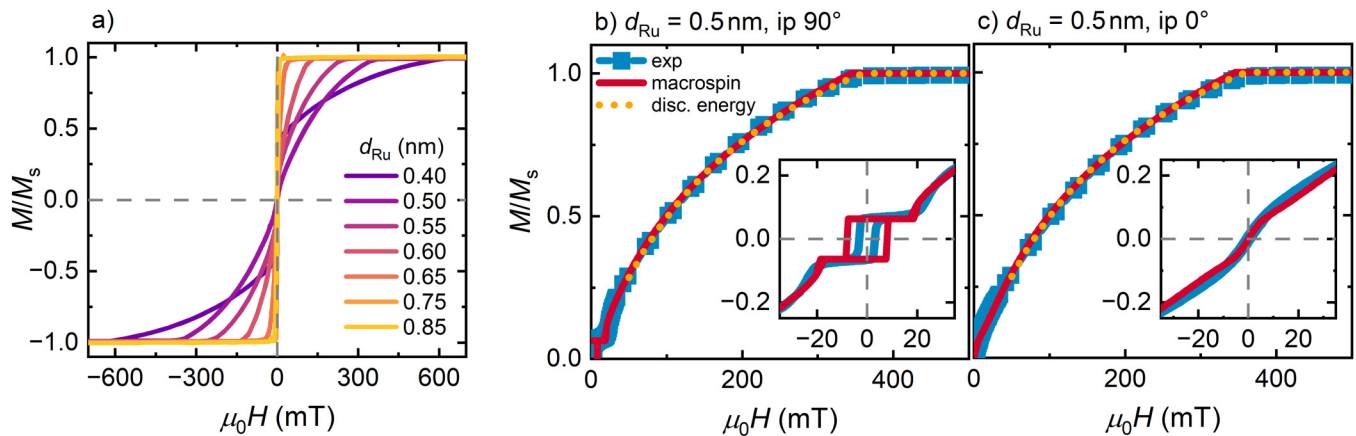


FIG. 3. (a) Experimental magnetic hysteresis loops of LiNbO₃/CoFeB(5)/Ru(d_{Ru})/CoFeB(5)/Si₃N₄(3) (thicknesses in nm) for various Ru thicknesses (0.4–0.85 nm) measured along the ip 0° direction, showing the evolution of saturation field with spacer thickness. Experimental data and model fits for $d_{Ru} = 0.5 \text{ nm}$ along (b) ip 90° and (c) ip 0° orientations, with insets showing $M(H)$ dependence around the zero external magnetic field.

distance is roughly 20 cm. Since all samples have a size of either $2.1 \times 3.1 \text{ mm}^2$ or $2.8 \times 3.8 \text{ mm}^2$, shape anisotropy is also negligible with respect to an in-plane anisotropy. Finally, there are also reports of this unexpected uniaxial magnetic anisotropy for sputter-deposited FM materials on LiNbO_3 substrates.^{38,58–61} However, it is partly ignored or referred to as having a magnetoelastic origin due to the anisotropic thermal expansion coefficient of LiNbO_3 substrates. In that case, the EA direction would depend on the anisotropy of the thermal expansion coefficients of the substrate and the sign of the magnetoelastic coupling constant of the magnetic material. The sign of the magnetoelastic coupling of polycrystalline Fe and Ni is reported to be the same,⁶² leading to the same in-plane easy axis on the same substrate, if the magnetoelastic coupling were the origin of the anisotropy. However, Ito *et al.*⁵⁹ report a hard axis along the X direction for polycrystalline Fe, while contrary to that, Yamaguchi *et al.*⁶⁰ found the easy axis along X for a Ni thin film. In both reports, the films were sputter-deposited at room temperature on 128° Y-cut LiNbO_3 . Another report finds the in-plane hard axis of $\text{Co}_{40}\text{Fe}_{40}\text{B}_{20}$ on 128° Y-cut LiNbO_3 to lie along X,⁵⁸ while we instead find the easy axis along X for our $\text{Co}_{40}\text{Fe}_{40}\text{B}_{20}/\text{Ru}/\text{Co}_{40}\text{Fe}_{40}\text{B}_{20}$ SAFs on Y-cut LiNbO_3 . For some ferromagnetic materials deposited on semiconductors like GaAs, it is proposed that the in-plane uniaxial magnetic anisotropy can be explained via a bond-orientational anisotropy.^{63–66} This could be an alternative origin for the observed uniaxial magnetic anisotropy.

Another question is where does the difference in the magnetic moment of the layers come from? Even though both CoFeB layers were deposited with the same sputter power and deposition time, the remanence magnetization is not zero [see Fig. 3(b)], hence suggesting an asymmetry of $d^A M_s^A \neq d^B M_s^B$. We assume that the saturation magnetizations are equal in both layers but that the LiNbO_3 substrate introduces a magnetic dead layer (MDL) in the bottom CoFeB layer, effectively reducing the magnetically active layer thickness. For all samples, one layer seems to be around 0.5 nm thinner than the other. For CoFeB on SiO_2 , an MDL of 0.7 nm has been reported,⁶⁷ so an MDL of around 0.5 nm on LiNbO_3 seems to be a reasonable assumption. Additionally, resputtering effects from the Ru deposition could also reduce the thickness of the bottom CoFeB layer.

Now, let us look into the bilinear and biquadratic IEC strengths. All $\text{CoFeB}(5)/\text{Ru}(d_{\text{Ru}})/\text{CoFeB}(5)$ SAF samples have been fitted with our MagSAF software as well as with the discrete energy model. An example is presented in Figs. 3(b) and 3(c). The fits of both models match the experimental data exceptionally well. With the current version of the discrete energy model, it is not possible to simulate full hysteresis loops. Because of this, its fit starts at a low field value and finishes at saturation. Contrary to that, MagSAF is capable of simulating full magnetic hysteresis loops and, despite its simple nature, it describes the reversal behavior of this SAF remarkably well. The fits of both models for all samples and details about the fitting procedure are given in the [supplementary material](#). From those fits, the bilinear and biquadratic IEC strengths are obtained for all samples (see Fig. 4). For the bilinear IEC strength, we see the expected oscillating behavior with a maximum antiferromagnetic coupling at $d_{\text{Ru}} \approx 0.40 \text{ nm}$, ferromagnetic coupling for $d_{\text{Ru}} = 0.75 \text{ nm}$, and again antiferromagnetic coupling starting at $d_{\text{Ru}} = 0.85 \text{ nm}$. The bilinear coupling strength cannot be

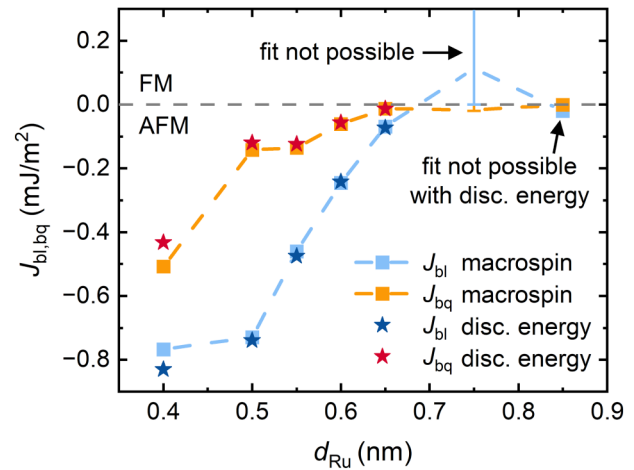


FIG. 4. Bilinear J_{bi} and biquadratic J_{bq} coupling strengths obtained from the macrospin model with our MagSAF software as well as from the discrete energy model for the $\text{CoFeB}(5)/\text{Ru}(d_{\text{Ru}})/\text{CoFeB}(5)$ thickness series. The sample with $d_{\text{Ru}} = 0.75 \text{ nm}$ is coupled ferromagnetically ($J_{\text{bi}} > 0$) and its coupling strengths cannot be obtained with either of the models. For $d_{\text{Ru}} = 0.85 \text{ nm}$, the coupling strength is too low to fit the magnetic hysteresis loop with the discrete energy model in its current state.

obtained for the sample with ferromagnetic coupling since the magnetic moments of both layers reverse together as one layer independent of the coupling strength. This uncertainty in the bilinear coupling strength is indicated by an error bar without a data point for the SYM sample with $d_{\text{Ru}} = 0.75 \text{ nm}$ in Fig. 4. However, if the layers would have different (non-zero) in-plane magnetic anisotropies, then the ferromagnetic coupling strength will affect the $M(H)$ loop. Since we assume that only the bottom CoFeB layer possesses an in-plane anisotropy, it is possible to fit the magnetic hysteresis loop with MagSAF but the values for the bilinear coupling are arbitrary. Because of this, the biquadratic coupling can also not be determined. The sample with the thickest Ru spacer layer with 0.85 nm possesses such a small antiferromagnetic coupling strength that fitting its magnetic hysteresis loop with the discrete energy model was not possible. The strongest antiferromagnetic bilinear coupling of $J_{\text{bi}} = -0.768 \text{ mJ/m}^2$ is in the range of literature values of $-0.41 \text{ mJ/m}^2 \approx J_{\text{bi}}^{\text{lit}} \approx -1.68 \text{ mJ/m}^2$ for similar SAFs.^{26,28,39} Our biquadratic coupling values are also similar to literature values.^{26,28} One reason for the wide spread in $J_{\text{bi}}^{\text{lit}}$ could be the roughness-induced Néel “orange-peel” coupling, which favors ferromagnetic alignment for in-plane magnetized films.¹⁷ If this is present, it reduces the total antiferromagnetic coupling strength. Besides the interface roughness and film morphology, the sputter target material quality can also influence the achievable coupling strengths.

However, most importantly, as revealed in Fig. 4, the bilinear and biquadratic coupling strengths obtained from the macrospin-based MagSAF software are almost identical to the ones obtained from the discrete energy model. Only for the sample with $d_{\text{Ru}} = 0.4 \text{ nm}$, a more notable difference between the two models becomes apparent. This can be explained by the stronger total

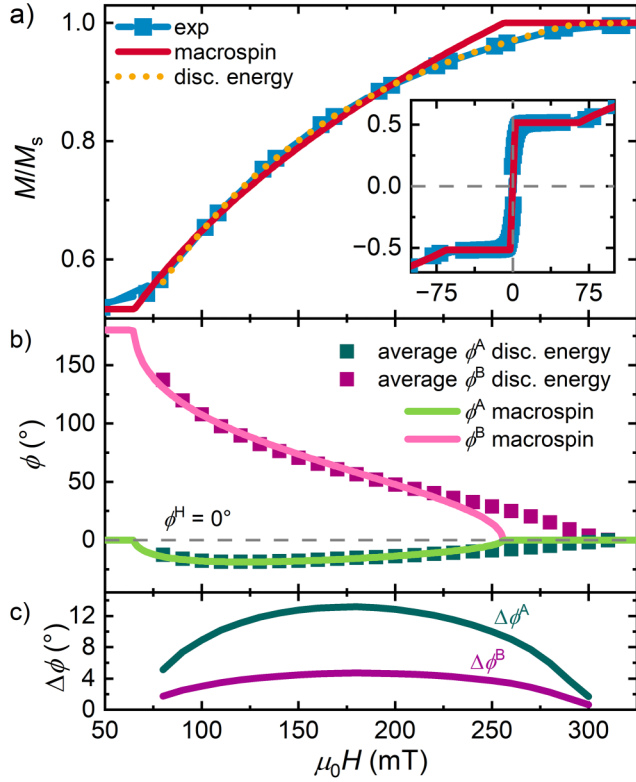


FIG. 5. (a) Magnetic hysteresis loop of sample ASYM and its fits with the macrospin and discrete energy model. The layer-resolved (average) angles of the magnetic moments, which are the backbone of the simulations, are shown in (b) for the macrospin and discrete energy model. The discrete energy model takes spin twisting over the ferromagnetic film thickness into account. (c) Angular difference $\Delta\phi$ between interface and surface spins in each FM layer, demonstrating significant spin twisting in the 18 nm thick layer A (up to 13.2°) vs minimal twisting in the 5.75 nm thin layer B (max 4.7°).

IEC leading to a more pronounced twisting of the spins over the FM layer thickness. In general, this twisting effect becomes more apparent for thicker ferromagnetic layers, higher saturation magnetizations, lower exchange stiffnesses, and stronger bilinear and biquadratic coupling. Apparently, the twisting effect becomes relevant for $|J_{\text{eff}}| \gtrsim 1.7 \text{ mJ/m}^2$ when $d^A = d^B \approx 5 \text{ nm}$,

$M_s^A = M_s^B \approx 1200 \text{ kA/m}$, and $A_{\text{ex}} \approx 15\text{--}20 \text{ pJ/m}$. For weaker IEC, we see that the bilinear and biquadratic coupling strengths can be reliably extracted with the macrospin-based MagSAF software.

B. Thick asymmetric SAF

To further investigate the spin twisting effect with FM layer thickness, we investigated the asymmetric SAF sample (ASYM) with the nominal layer stack of sub/Ta(2)/Ru(2)/CoFeB(19)/Ru(0.55)/CoFeB(6)/Si₃N₄(3). An x-ray reflectivity measurement revealed that the CoFeB thicknesses deviate slightly with $d^A = 18.08 \text{ nm}$ and $d^B = 5.74 \text{ nm}$ (see the [supplementary material](#)). Because of this, the thicknesses were set to $d^A = 18.0 \text{ nm}$ and $d^B = 5.75 \text{ nm}$ to be a multiple of the CoFeB lattice spacing $a = 0.25 \text{ nm}$,^{52,53} which is required for the discrete energy model. In Fig. 5(a), the magnetic hysteresis loop along the ip 0° direction and its fits with the macrospin and discrete energy model are shown. Even though the macrospin fit is overall good, it fails to correctly describe the magnetic behavior close to saturation. This is a characteristic feature indicating significant twisting of the spins over the thickness of the relatively thick CoFeB(18) layer. Figure 5(b) shows the layer-resolved angles of the magnetic moments for both models, which are the backbones of the simulated magnetic hysteresis loops. For the discrete energy model, the average of the sublayer angles is shown. We can see satisfactory agreement between the two models up to roughly 200 mT after which the macrospin model starts to saturate too early. In Fig. 5(c), we plot the angle difference $\Delta\phi$ between the sublayer spin angle at the Ru interface and the one on the opposite side for each ferromagnetic layer for the discrete energy model. In the thin layer B with $d^B = 5.75 \text{ nm}$, the twisting is almost negligible with the highest angle difference of 4.7° , while the thicker layer A with $d^A = 18.0 \text{ nm}$ has a more pronounced twisting effect with a maximum angle difference of 13.2° . This makes it impossible for the macrospin model to perfectly describe the magnetic reversal behavior. It also manifests itself in a larger difference in the fitted IEC strengths between the two models (see Table II). Note that the magnetic hysteresis loop was additionally measured along the ip 90° direction and that both measurements were fitted in parallel. While the bilinear coupling J_{bl} values are very close to each other, it is a considerable amount higher ($\approx 40\%$) than any of the SYM samples. The ASYM SAF was fabricated and measured one year before the others, and for its fabrication, other CoFeB and Ru sputter targets were used (see Sec. III). Either differences in the

TABLE II. Extracted sample parameters for samples SYM2 and ASYM. The M_s values were obtained from SQUID-VSM measurements and were set constant during the fits. For the discrete energy fits, the thicknesses d^A and d^B were chosen based on the requirement of being multiples of the lattice spacing $a = 0.25 \text{ nm}$.^{52,53} The standard error in the J_{bl} and J_{bq} values obtained from the discrete energy model was $<0.005 \text{ mJ/m}^2$.

Sample	Model	d^A (nm)	d_{Ru} (nm)	d^B (nm)	M_s (kA/m)	J_{bl} (mJ/m ²)	J_{bq} (mJ/m ²)	A_{ex} (pJ/m)	ϕ_{ani}^B (deg)	$\mu_0 H_{\text{ani}}^B$ (mT)
SYM2	Macrospin	5.32	0.50	4.68	1179.6	-0.729	-0.142	$+\infty$	90	1.66
SYM2	Discrete energy	5.25	0.50	4.75	1179.6	-0.740	-0.120	20.4 ± 1.3	90	1.54
ASYM	Macrospin	18.00	0.55	5.75	1251.1	-1.045	-0.174	$+\infty$	90	1.54
ASYM	Discrete energy	18.00	0.55	5.75	1251.1	-1.062	-0.088	17.9 ± 0.4	90	1.54

sputter target quality or roughness-induced Néel coupling could be an explanation for this difference in the J_{bl} coupling strength. XRR measurements support the latter of the two possibilities (see the [supplementary material](#)). Besides that, the two models yield quite different biquadratic coupling values of $J_{bq} = -0.174 \text{ mJ/m}^2$ (macrospin) vs $J_{bq} = -0.088 \text{ mJ/m}^2$ and $A_{ex} = 17.9 \text{ pJ/m}$ (discrete energy). In the discrete energy model, J_{bq} and A_{ex} are strongly correlated: increasing J_{bq} or decreasing A_{ex} enhances the curvature of $M(H)$.⁴⁰ By contrast, the macrospin model assumes an infinite A_{ex} so the fit inevitably overestimates J_{bq} to compensate for the missing A_{ex} contribution to the curvature. However, with broader fit boundaries for the exchange stiffness ($5 \leq A_{ex} \leq 50 \text{ pJ/m}$ instead of $8 \leq A_{ex} \leq 23 \text{ pJ/m}$), fit results closer to the macrospin model have been obtained with $J_{bq} = -0.129 \text{ mJ/m}^2$ and $A_{ex} = 24.9 \text{ pJ/m}$. Since the biquadratic coupling and exchange stiffness are correlated parameters in the discrete energy model, the exact deviation from the macrospin model is difficult to quantify.

V. CONCLUSIONS

The macrospin-based software MagSAF was introduced and tested on a CoFeB(5)/Ru(d_{Ru})/CoFeB(5) SAF thickness series with $0.40 \text{ nm} \leq d_{Ru} \leq 0.85 \text{ nm}$ by fitting their magnetic hysteresis loops and comparing the result with the discrete energy model from Wadge *et al.*⁴⁰ For most of our samples, we found excellent agreement between the extracted bilinear and biquadratic coupling strengths from the two models. This suggests that MagSAF is at least suitable for extracting the bilinear and biquadratic IEC strengths for synthetic antiferromagnets with $d^{A,B} \lesssim 5 \text{ nm}$, $M_s \lesssim 1200 \text{ kA/m}$, $|J_{eff}| \lesssim 1.0 \text{ mJ/m}^2$, and $A_{ex} \gtrsim 15\text{--}20 \text{ pJ/m}$. For our thinnest Ru thickness of $d_{Ru} = 0.4 \text{ nm}$, the expected increase in biquadratic coupling lead to a huge increase in J_{eff} , which resulted in a moderate difference between the macrospin and discrete energy model due to the spin twisting over the ferromagnetic layer thickness. Additionally, we investigated an asymmetric CoFeB(18.0)/Ru(0.55)/CoFeB(5.75) SAF. We found that the more pronounced spin twisting effect in the relatively thick CoFeB(18) layer led to a larger deviation in the extracted biquadratic coupling values between the two models, which demonstrates the limitations of the macrospin model.

The simple nature of the macrospin model allows the spin rotation during a magnetic hysteresis loop to be understood easily and quickly. Its low computational cost and the possibility to simulate and fit the complete magnetic reversal behavior are additional advantages. All of this is combined in our open-source software MagSAF, which gives researchers the opportunity to quickly extract the bilinear and biquadratic interlayer exchange coupling strengths, any in-plane uniaxial magnetic anisotropies as well as any asymmetry in the thickness or saturation magnetization of the two ferromagnetic layers.

SUPPLEMENTARY MATERIAL

See the [supplementary material](#) for a detailed description of the fitting procedures of both models (macrospin and discrete energy), insight into some fit results of the macrospin model, information on how to determine the quality of the fitted J_{bl} and J_{bq} parameters, the extracted coupling strengths for all samples, x-ray

reflectivity measurements for all samples, and $2\theta/\omega$ x-ray diffraction measurements of a blank Y-cut LiNbO₃ substrate as well as samples ASYM and SYM7.

ACKNOWLEDGMENTS

The project was partly funded by the Deutsche Forschungsgemeinschaft (DFG, German Research Foundation)—Projektnummern 470034807 and 492421737.

AUTHOR DECLARATIONS

Conflict of Interest

The authors have no conflicts to disclose.

Author Contributions

Stephan Glamsch: Data curation (lead); Formal analysis (lead); Investigation (lead); Software (lead); Visualization (lead); Writing – original draft (lead); Writing – review & editing (equal). **Matthias Küif:** Conceptualization (supporting); Software (supporting); Supervision (equal); Writing – review & editing (equal). **Afan Terko:** Formal analysis (supporting); Validation (equal); Writing – review & editing (equal). **Andreas Hörner:** Resources (supporting); Writing – review & editing (equal). **Erol Girt:** Formal analysis (supporting); Validation (equal); Writing – review & editing (equal). **Manfred Albrecht:** Conceptualization (lead); Funding acquisition (lead); Resources (lead); Supervision (equal); Writing – review & editing (equal).

DATA AVAILABILITY

The data that support the findings of this study are available from the corresponding author upon reasonable request.

REFERENCES

- 1M. D. Stiles, *Phys. Rev. B* **48**, 7238 (1993).
- 2P. Bruno, *Phys. Rev. B* **52**, 411 (1995).
- 3M. A. Ruderman and C. Kittel, *Phys. Rev.* **96**, 99 (1954).
- 4T. Kasuya, *Prog. Theor. Phys.* **16**, 45 (1956).
- 5K. Yosida, *Phys. Rev.* **106**, 893 (1957).
- 6M. Rührig, R. Schäfer, A. Hubert, R. Mosler, J. A. Wolf, S. Demokritov, and P. Grünberg, *Phys. Status Solidi A* **125**, 635 (1991).
- 7J. C. Slonczewski, *Phys. Rev. Lett.* **67**, 3172 (1991).
- 8J. C. Slonczewski, *J. Appl. Phys.* **73**, 5957 (1993).
- 9Z. Nunn, C. Abert, D. Suess, and E. Girt, *Sci. Adv.* **6**, eabd8861 (2020).
- 10C. Abert, S. Koraltan, F. Bruckner, F. Slanovc, J. Lisik, P. Omelchenko, E. Girt, and D. Suess, *Phys. Rev. B* **106**, 054401 (2022).
- 11S. Demokritov, E. Tsymlal, P. Grünberg, W. Zinn, and I. K. Schuller, *Phys. Rev. B* **49**, 720 (1994).
- 12J. F. Bobo, H. Kikuchi, O. Redon, E. Snoeck, M. Piecuch, and R. L. White, *Phys. Rev. B* **60**, 4131 (1999).
- 13*Ultrathin Magnetic Structures III: Fundamentals of Nanomagnetism*, edited by J. A. C. Bland and B. Heinrich (Springer, Berlin, 2005).
- 14S. O. Demokritov, *J. Phys. D: Appl. Phys.* **31**, 925 (1998).
- 15L. Néel, C. R. Hebd. Seances Acad. Sci. **255**, 1676 (1962), available at <https://hal.science/hal-02878443v1>.
- 16L. Néel, C. R. Hebd. Seances Acad. Sci. **255**, 1545 (1962), available at <https://hal.science/hal-02878442v1>.

- ¹⁷M. A. Kuznetsov, O. G. Udalov, and A. A. Fraerman, *J. Magn. Magn. Mater.* **474**, 104 (2019).
- ¹⁸S. Pietambaram, J. Janesky, R. Dave, J. Sun, G. Steiner, and J. Slaughter, *IEEE Trans. Magn.* **40**, 2619 (2004).
- ¹⁹J. C. A. Huang, C. Y. Hsu, S. F. Chen, C. P. Liu, Y. F. Liao, M. Z. Lin, and C. H. Lee, *J. Appl. Phys.* **101**, 123923 (2007).
- ²⁰T. Takenaga, H. Takada, S. Tomohisa, T. Furukawa, T. Kuroiwa, and K. Yoshiara, *J. Appl. Phys.* **105**, 07C310 (2009).
- ²¹S. Bandiera, R. C. Sousa, S. Auffret, B. Rodmacq, and B. Dieny, *Appl. Phys. Lett.* **101**, 072410 (2012).
- ²²K. Yakushiji, A. Sugihara, A. Fukushima, H. Kubota, and S. Yuasa, *Appl. Phys. Lett.* **110**, 092406 (2017).
- ²³C.-L. Yang and C.-H. Lai, *Sci. Rep.* **11**, 15214 (2021).
- ²⁴C.-W. Cheng, T.-I. Cheng, C. H. Shiue, C.-L. Weng, Y.-C. Tsai, and G. Chern, *IEEE Trans. Magn.* **49**, 4433 (2013).
- ²⁵P. Pirro, A. Hamadeh, M. Lavanant-Jambert, T. Meyer, B. Tao, E. Rosario, Y. Lu, M. Hehn, S. Mangin, and S. Petit Watelot, *J. Magn. Magn. Mater.* **432**, 260 (2017).
- ²⁶A. Hashimoto, S. Saito, D. Y. Kim, H. Takashima, T. Ueno, and M. Takahashi, *IEEE Trans. Magn.* **42**, 2342 (2006).
- ²⁷W. X. Xia, K. Inoue, S. Saito, and M. Takahashi, *J. Phys.: Conf. Ser.* **266**, 012064 (2011).
- ²⁸O. Gladii, R. Salikhov, O. Hellwig, H. Schultheiss, J. Lindner, and R. A. Gallardo, *Phys. Rev. B* **107**, 104419 (2023).
- ²⁹M. Belmeguenai, T. Martin, G. Woltersdorf, M. Maier, and G. Bayreuther, *Phys. Rev. B* **76**, 104414 (2007).
- ³⁰A. Zaleski, W. Skowronski, M. Czapkiewicz, J. Kanak, T. Stobiecki, R. Macedo, S. Cardoso, and P. P. Freitas, *J. Phys.: Conf. Ser.* **200**, 052035 (2010).
- ³¹O. Wojewoda, J. Holobrádek, D. Pavelka, E. Pribytova, J. Krčma, J. Klíma, J. Panda, J. Michalička, T. Lednický, A. V. Chumak, and M. Urbánek, *Appl. Phys. Lett.* **125**, 132401 (2024).
- ³²P. D. Kulkarni and T. Nakatani, *Appl. Phys. Lett.* **125**, 162405 (2024).
- ³³R. R. Gareev, D. E. Bürgler, M. Buchmeier, R. Schreiber, and P. Grünberg, *J. Magn. Magn. Mater.* **240**, 235 (2002).
- ³⁴M. Desai, A. Misra, and W. Doyle, *IEEE Trans. Magn.* **41**, 3151 (2005).
- ³⁵B. K. Kuanr, M. Buchmeier, R. R. Gareev, D. E. Bürgler, R. Schreiber, and P. Grünberg, *J. Appl. Phys.* **93**, 3427 (2003).
- ³⁶M. Buchmeier, B. K. Kuanr, R. R. Gareev, D. E. Bürgler, and P. Grünberg, *Phys. Rev. B* **67**, 184404 (2003).
- ³⁷E. Girt, W. Huttema, O. N. Mryasov, E. Montoya, B. Kardasz, C. Eyrih, B. Heinrich, A. Yu. Dobin, and O. Karis, *J. Appl. Phys.* **109**, 07B765 (2011).
- ³⁸A. Mouhoub, F. Millo, C. Chappert, J.-V. Kim, J. Létang, A. Solignac, and T. Devolder, *Phys. Rev. Mater.* **7**, 044404 (2023).
- ³⁹T. McKinnon, "Study of magnetic interlayer coupling in synthetic antiferromagnets for use in MRAM devices," Ph.D. thesis (Simon Fraser University, 2020).
- ⁴⁰E. Wadge, A. Terko, G. Lertzman-Lepofsky, P. Omelchenko, B. Heinrich, M. Rojas, C. Abert, and E. Girt, *Phys. Rev. B* **110**, 174417 (2024).
- ⁴¹J. Jiménez-Bustamante, A. Lindner, H. N. Koyun, R. Salikhov, K. Lenz, J. Lindner, and R. A. Gallardo, *Phys. Rev. B* **109**, 094403 (2024).
- ⁴²T. McKinnon, B. Heinrich, and E. Girt, *J. Magn. Magn. Mater.* **546**, 168646 (2022).
- ⁴³C. Muehlenhoff, C. Vogler, W. Raberg, D. Suess, and M. Albrecht, *IEEE Sens. J.* **21**, 13176 (2021).
- ⁴⁴M. Küß, S. Glamsch, Y. Kunz, A. Hörner, M. Weiler, and M. Albrecht, *ACS Appl. Electron. Mater.* **5**, 5103 (2023).
- ⁴⁵M. Küß, S. Glamsch, A. Hörner, and M. Albrecht, *ACS Appl. Electron. Mater.* **6**, 1790 (2024).
- ⁴⁶See <https://github.com/stephan-glamsch/MagSAF> for the documentation and access to the source code of our software MagSAF.
- ⁴⁷P. Virtanen, R. Gommers, T. E. Oliphant, M. Haberland, T. Reddy, D. Cournapeau, E. Burovski, P. Peterson, W. Weckesser, J. Bright, S. J. van der Walt, M. Brett, J. Wilson, K. J. Millman, N. Mayorov, A. R. J. Nelson, E. Jones, R. Kern, E. Larson, C. J. Carey, Í. Polat, Y. Feng, E. W. Moore, J. VanderPlas, D. Laxalde, J. Perktold, R. Cimrman, I. Henriksen, E. A. Quintero, C. R. Harris, A. M. Archibald, A. H. Ribeiro, F. Pedregosa, and P. van Mulbregt, *Nat. Methods* **17**, 261 (2020).
- ⁴⁸J. Nocedal and S. J. Wright, in *Numerical Optimization*, 2nd ed., Springer Series in Operations Research and Financial Engineering (Springer, New York, 2006), p. 168.
- ⁴⁹S. G. Nash and J. Nocedal, *SIAM J. Optim.* **1**, 358 (1991).
- ⁵⁰A.-O. Mandru, O. Yıldırım, M. A. Marioni, H. Rohrmann, M. Heigl, O.-T. Ciubotariu, M. Penedo, X. Zhao, M. Albrecht, and H. J. Hug, *J. Vac. Sci. Technol.* **38**, 023409 (2020).
- ⁵¹S. Sanna and W. G. Schmidt, *Phys. Rev. B* **81**, 214116 (2010).
- ⁵²M. Singh, P. Gupta, S. Rai, S. K. Vayalil, M. Gupta, I. Carlomagno, C. Meneghini, and A. Gupta, *Surf. Interfaces* **56**, 105716 (2025).
- ⁵³D. Kirk, A. Kohn, K. B. Borisenko, C. Lang, J. Schmalhorst, G. Reiss, and D. J. H. Cockayne, *Phys. Rev. B* **79**, 014203 (2009).
- ⁵⁴H. J. Waring, N. A. B. Johansson, I. J. Vera-Marun, and T. Thomson, *Phys. Rev. Appl.* **13**, 034035 (2020).
- ⁵⁵D. Wen, J. Li, G. Gan, Y. Yang, H. Zhang, and Y. Liu, *Mater. Res. Bull.* **110**, 107 (2019).
- ⁵⁶X. Wen, B. Wang, P. Sheng, S. Hu, H. Yang, K. Pei, Q. Zhan, W. Xia, H. Xu, and R.-W. Li, *Appl. Phys. Lett.* **111**, 142403 (2017).
- ⁵⁷L. Yuan, B. Wang, D. Zha, C. Liu, M. Li, Y. Xie, H. Yang, Y. Cao, H. Xu, and R.-W. Li, *AIP Adv.* **12**, 045203 (2022).
- ⁵⁸R. L. Seeger, F. Millo, A. Mouhoub, G. De Loubens, A. Solignac, and T. Devolder, *Phys. Rev. Mater.* **7**, 054409 (2023).
- ⁵⁹M. Ito, S. Ono, H. Fukui, K. Kogirima, N. Maki, T. Hikage, T. Kato, T. Ohkochi, A. Yamaguchi, M. Shima, and K. Yamada, *J. Magn. Magn. Mater.* **564**, 170177 (2022).
- ⁶⁰A. Yamaguchi, T. Ohkochi, M. Oura, K. Yamada, T. Saiki, S. Suzuki, Y. Utsumi, and A. Nakao, *Nanomaterials* **11**, 1024 (2021).
- ⁶¹M. Ito, A. Yamaguchi, D. Oshima, T. Kato, M. Shima, and K. Yamada, *Appl. Phys. Lett.* **119**, 152407 (2021).
- ⁶²E. Klokholm and J. Aboaf, *J. Appl. Phys.* **53**, 2661 (1982).
- ⁶³A. T. Hindmarch, A. W. Rushforth, R. P. Champion, C. H. Marrows, and B. L. Gallagher, *Phys. Rev. B* **83**, 212404 (2011).
- ⁶⁴G. Bayreuther, J. Prempfer, M. Sperl, and D. Sander, *Phys. Rev. B* **86**, 054418 (2012).
- ⁶⁵H. Tu, J. Wang, L. Wei, Y. Yuan, W. Zhang, B. You, and J. Du, *AIP Adv.* **8**, 056101 (2018).
- ⁶⁶Y. Yan, B. Liu, X. Lu, J. Wang, S. S. Dhesi, I. G. Will, V. K. Lazarov, J. Du, J. Wu, R. Zhang, and Y. Xu, *Appl. Phys. Lett.* **126**, 092410 (2025).
- ⁶⁷K. Oguz, P. Jivrajka, M. Venkatesan, G. Feng, and J. M. D. Coey, *J. Appl. Phys.* **103**, 07B526 (2008).